Concerted actions of distinct nonmuscle myosin II isoforms drive intracellular membrane remodeling in live animals

Oleg Milberg,[2*] Akiko Shitara,[1,2*] Seham Ebrahim,[1*] Andrius Masedunskas,[2,5] Muhibullah Tora,[2] Duy T. Tran,[3] Yun Chen,[1] Mary Anne Conti,[4] Robert S. Adelstein,[4] Kelly G. Ten Hagen,[3] and Roberto Weigert[1,2]

[1]Laboratory of Cellular and Molecular Biology, Center for Cancer Research, National Cancer Institute, [2]Intracellular Membrane Trafficking Section, [3]Developmental Glycobiology Section, National Institute of Dental and Craniofacial Research, and [4]Laboratory of Molecular Cardiology, National Heart, Lung, and Blood Institute, National Institutes of Health, Bethesda, MD
[5]School of Medical Sciences, University of New South Wales, Sidney, Australia

Membrane remodeling plays a fundamental role during a variety of biological events. However, the dynamics and the molecular mechanisms regulating this process within cells in mammalian tissues in situ remain largely unknown. In this study, we use intravital subcellular microscopy in live mice to study the role of the actomyosin cytoskeleton in driving the remodeling of membranes of large secretory granules, which are integrated into the plasma membrane during regulated exocytosis. We show that two isoforms of nonmuscle myosin II, NMIIA and NMIIB, control distinct steps of the integration process. Furthermore, we find that F-actin is not essential for the recruitment of NMII to the secretory granules but plays a key role in the assembly and activation of NMII into contractile filaments. Our data support a dual role for the actomyosin cytoskeleton in providing the mechanical forces required to remodel the lipid bilayer and serving as a scaffold to recruit key regulatory molecules.

Introduction

Membrane remodeling is essential for the regulation of a variety of events, ranging from organelle biogenesis to cell migration, cell division, and membrane trafficking. This process requires both continuous modifications of the composition and the properties of the lipid bilayer (Shnyrova et al., 2009; Kozlov et al., 2014) and the application of mechanical forces directly to the membranes. The forces are provided by cytoplasmic protein complexes (Daley and Yamada, 2013; Henne et al., 2013; Simunovic and Bassereau, 2014), which include curvature generators such as BAR (Bin/Amphiphysin/Rvs) domain–containing proteins (Kozlov et al., 2014; Suetsugu et al., 2014), the ESCRT (endosomal sorting complexes required for transport) complex (Henne et al., 2013; Chiaruttini et al., 2015), fission factors such as the large GTPase dynamin (Ferguson and De Camilli, 2012), and various components of the actomyosin cytoskeleton (Hatch et al., 2014; Korobova et al., 2014). Although membrane remodeling has been extensively studied in cell-free systems and cultured cells, information about the dynamics, mechanisms, and molecular players that drive and regulate this process in multicellular organisms in vivo, where the three-dimensional architecture, cell–cell interactions, and cues coming from vasculature and nervous systems likely have key effects (Shitara and Weigert, 2015), remains sparse. To address this, we established an in vivo model system to study the role of the actomyosin cytoskeleton in membrane remodeling during regulated exocytosis, a fundamental process in secretory organs (Burgoyne and Morgan, 2003; Sokac et al., 2003; Jerdeva et al., 2005; Nightingale et al., 2011; Miklavc et al., 2012; Porat-Shliom et al., 2013). Using intravital subcellular microscopy (ISMic), a light microscopy–based technique that enables imaging intracellular structures in live animals (Pittet and Weissleder, 2011; Weigert et al., 2013), we previously investigated the remodeling of secretory granules in the acinar cells of rodent submandibular salivary glands (SGs; Masedunskas et al., 2011a; Milberg et al., 2014). We showed that, after the granules release their contents into the extracellular space, their membranes gradually integrate into the apical plasma membrane (APM). This remodeling process is triggered by the assembly of an actomyosin complex comprising F-actin and two isoforms of the actin-binding motor nonmuscle myosin II, NMIIA and NMIIB (Fig. 1 A; Masedunskas et al., 2011a). Using a pharmacological approach, we determined that both F-actin assembly and NMII contractile activity were required to drive the integra-

*O. Milberg, A. Shitara, and S. Ebrahim contributed equally to this paper.

Correspondence to Roberto Weigert: weigertr@mail.nih.gov

Abbreviations used: ADF, actin-depolymerizing factor; APM, apical plasma membrane; ISMic, intravital subcellular microscopy; ISOP, isoproterenol; LF, Lifeact; MLCK, myosin light chain kinase; RLC, regulatory light chain; SC, subcutaneously; SG, salivary gland.

The Rockefeller University Press
J. Cell Biol. Vol. 216 No. 7 1925–1936
https://doi.org/10.1083/jcb.201612126

tion to completion (Masedunskas et al., 2011a,b, 2012a,b). In the current study, we sought to: (a) determine the isoform-specific roles of NMII in controlling this process and (b) elucidate the mechanisms underlying their assembly into contractile filaments on the granules.

Results and discussion

To investigate isoform-specific roles of NMII in regulated exocytosis, we used homozygous floxed NMIIA ($IIA^{fl/fl}$), NMIIB ($IIB^{fl/fl}$), or NMIIA/NMIIB ($IIA/IIB^{fl/fl}$) mice (Fig. S1; Crish et al., 2013). These strains were crossed with mice expressing the Cre recombinase (Cre) reporter $Rosa^{mT/mGFP}$ (mT/mGFP) in which a plasma membrane–targeted peptide tagged with the tandem-tomato protein (mT) is replaced by a similar peptide tagged with GFP (mGFP) upon Cre expression (Fig. S1; Muzumdar et al., 2007). Both probes are localized at the APM and diffuse into the membranes of the granules upon opening of the fusion pore, thus providing the contrast to visualize the secretory granules and to study the kinetics of their integration (Fig. S1; Masedunskas et al., 2011a). An adenovirus engineered to express Cre (Ade-Cre) was delivered to the SGs by retroinjection into the salivary ducts of anesthetized mice (Sramkova et al., 2009). Transfected acinar cells located within the first 50 µm from the gland surface were readily identified and imaged using ISMic (Fig. S1). The extent of the depletion of NMIIA and NMIIB was assessed by immunocytochemistry (Fig. S2). In mT/mGFP mice, Cre expression did not affect the levels of NMIIA and NMIIB (Fig. S2 A). In the NMII flox mice, although we observed variability in the levels of staining and the background levels, we estimated that after 2 wk from the injection of the virus, NMII isoforms were depleted 60–90% with respect to adjacent acinar cells, which did not express the Cre recombinase (Fig. S2 A).

In mT/mGFP mice, Cre expression did not affect the morphology of the acinar cells (Fig. 1 B). To stimulate regulated exocytosis, we injected mice subcutaneously (SC) with low doses of the β-adrenergic agonist isoproterenol (ISOP; 0.01–0.03 mg/kg; Masedunskas et al., 2011a). The kinetics of granule integration into the APM were estimated by measuring the diameter of the fused secretory granules over time, as described in Materials and methods (Fig. S1 and Fig. 1, D–G). In both nontransfected and Cre-transfected control mice, granule membranes integrated into the APM within 40–50 s, with linear kinetics similar to those previously reported (Fig. 1, B and D; and Video 1; Masedunskas et al., 2011a). In $IIA/IIB^{fl/fl}$ mice, although the onset of exocytosis was not affected, we observed that the integration of the fused secretory granules into the APM was either significantly delayed or halted within the observation period of 150 s (Fig. 1, C and E; Fig. S2 B; and Video 1). The maximum granule diameter over this period was significantly increased in $IIA/IIB^{fl/fl}$ mice (Fig. 1 E, bottom). Although the kinetics of the integration exhibited some variability (Fig. S2 B), we consistently observed that the granules significantly expanded in diameter with respect to the nontransfected cells. As previously reported, the impairment of F-actin assembly results in a transient expansion of the secretory granules because of both the buildup of hydrostatic pressure inside the acinar canaliculi by fluids released during secretion and the stimulation of compound exocytosis (Masedunskas et al., 2011a, 2012a,b). The recruitment of F-actin at the APM and onto the secretory granules in $IIA/IIB^{-/-}$ cells was, however, not affected (Fig. S2 C), suggesting the phenotype observed was most likely caused by the lack of both NMII isoforms.

Interestingly, cells lacking either NMIIA or NMIIB showed distinct integration phenotypes. In Cre-transfected $IIA^{fl/fl}$ mice, secretory granules partially integrated into the APM (50–60% of the initial diameter) and then halted (Fig. 1 F; Fig. S2, B and D; and Video 1). However, in Cre-transfected $IIB^{fl/fl}$ mice, the secretory granules underwent an initial expansion, followed by a delayed integration (Fig. 1 G; Fig. S2, B and E; and Video 1). The maximum granule diameter over the course of integration was also significantly higher in $IIB^{fl/fl}$ mice (Fig. 1 G, bottom) but not affected in $IIA^{fl/fl}$ mice (Fig. 1 F, bottom). These findings show that both NMIIA and NMIIB are required to regulate the integration of the secretory granules into the APM and likely act at two different phases of this process. Although we cannot rule out that the impairment in granule integration occurs because of changes in the biophysical properties of the APM (e.g., membrane tension), we favor a model in which the two NMII isoforms generate contractile forces on the F-actin scaffold, which is assembled on the granules. The fact that a small population of granules undergoes integration in the absence of both isoforms could be because of the residual levels of NMII isoforms or additional mechanisms that may regulate this process. Indeed, it has recently been proposed that granule compression in alveolar type II cells is regulated by actin depolymerization and cross-linking (Miklavc et al., 2015). Consistent with this study, we observed that the F-actin–severing protein actin-depolymerizing factor (ADF)/cofilin is also recruited onto the granules after fusion with the APM (Fig. S3 E). We ruled out the involvement of the third isoform of NMII, NMIIC (Fig. S3 E), and are currently investigating other myosin motors, such as myosin 1c (Sokac et al., 2006).

Next, we determined the kinetics and the order of recruitment of both NMII isoforms and F-actin with respect to the opening of the fusion pore. To this end, we used: (a) transgenic mice that express the well-established F-actin probe Lifeact (LF) tagged with either GFP or RFP-Ruby (Fig. S3 A and Fig. 2; Riedl et al., 2008, 2010), (b) knock-in mice that express GFP-NMIIA or GFP-NMIIB (Fig. 2; Bao et al., 2007; Zhang et al., 2012), (c) mT/mGFP mice (Fig. S3 B), and (d) mice generated by crossing some of these strains (Fig. 3 and Fig. S3). Under resting conditions, GFP-LF, RFP-LF, GFP-NMIIA, and GFP-NMIIB localized primarily to the APM of the acinar cells and, to a lesser extent, to the basolateral plasma membrane (Fig. 2 A, arrows). Upon injection of ISOP, they appeared on secretory granules in close proximity to the APM (Fig. 2 B, arrowheads). Both GFP-NMIIA and GFP-NMIIB were present on ∼80% of F-actin–coated granules, indicating that both isoforms are recruited onto the same granules (Fig. 2 D). Quantitation of fluorescence intensity on the granules over time showed that the levels of LF, NMIIA, and NMIIB all increased in a linear fashion, with LF exhibiting a faster recruitment than both NMII isoforms, reaching a peak, and then declining (Fig. 2 B, arrowheads; Fig. 2 C; and Videos 2 and 3). We analyzed the order of recruitment and found that LF was detected on the granules ∼2 s after the appearance of the mT probe, which, as we have previously shown, occurs concomitantly with the opening of the fusion pore (Fig. S3; Masedunskas et al., 2011a). In mice expressing RFP-LF and either GFP-NMIIA or GFP-NMIIB, we found that both NMII isoforms appeared onto the fused granules with a delay of a

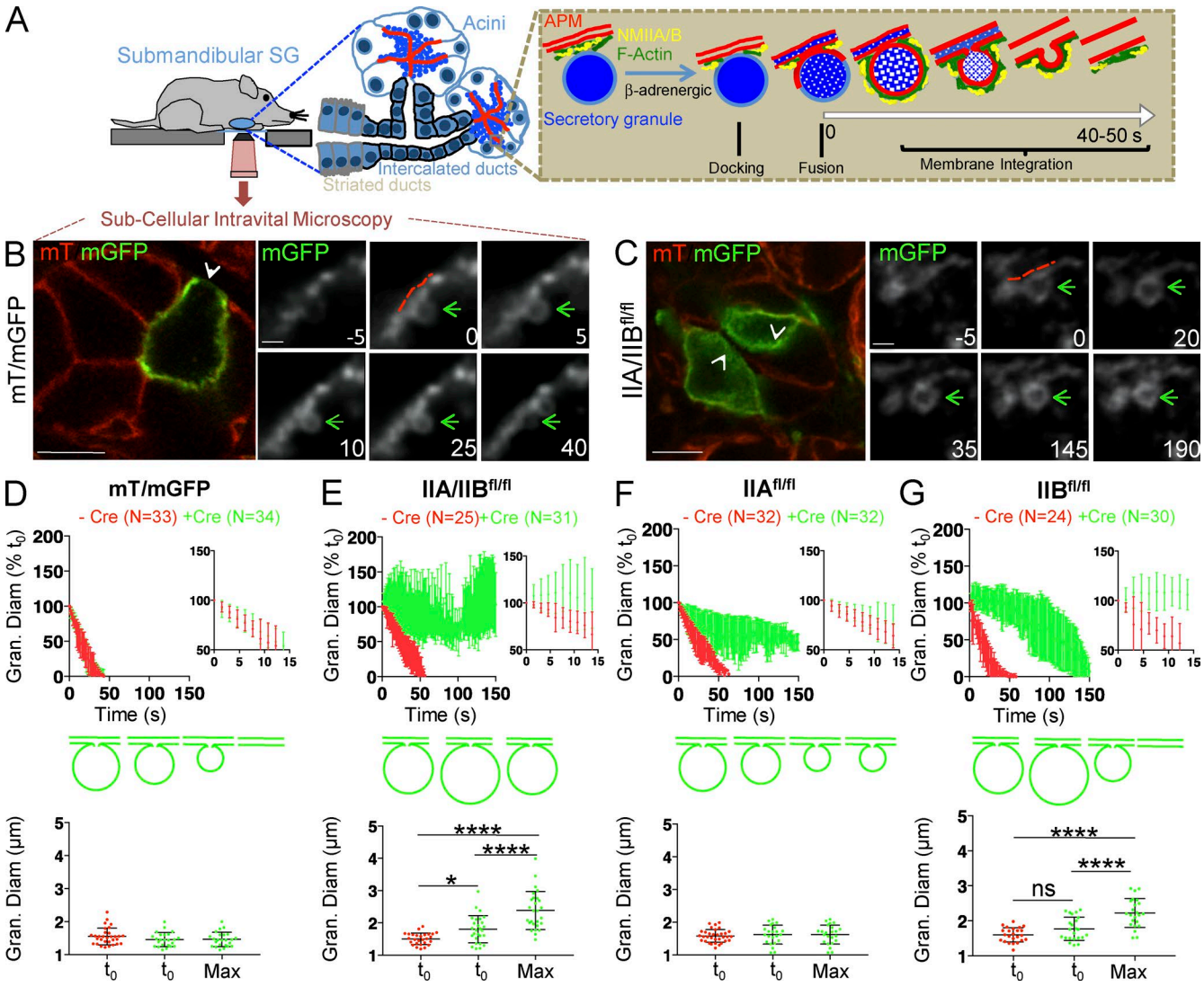

Figure 1. **NMIIA and NMIIB regulate the integration of the secretory granules into the APM.** (A) Diagram of the experimental set up and model of the integration of the secretory granules into the APM of acinar cells in submandibular SGs upon β-adrenergic stimulation. (B and C) ISMic of the SGs in mT/mGFP (B) and IIA/IIB$^{fl/fl}$ (C) mice after the expression of Ade-Cre. Low magnification of the Cre-transfected cell expressing mGFP (left, arrowheads; Bars, 20 µm) and time-lapse series of the integration of the secretory granules (right, green arrows; bars, 2 µm) with the APM (red dashed lines) are shown. Time 0 represents the point at which the limiting membranes of the granules were detected. (D–G) Quantitative analysis of the integration of the secretory granules in mT/mGFP (D), IIA/IIB$^{fl/fl}$ (E), IIA$^{fl/fl}$ (F), and IIB$^{fl/fl}$ (G) mice. (Top) The diameters of the granules were measured during the integration and reported as a function of time either in cells expressing (green curves) or not expressing (red curves) Cre. Insets show expansion of the first 15 s of integration. (Bottom) Mean granule diameter (Gran. Diam) ± SD at the onset of integration and mean maximum (Max) diameter measured over the course of the 150-s observation window ±SD in Cre$^+$ and Cre$^-$ cells. *, P < 0.05; ****, P < 0.0001; ANOVA. N = number of granules in 3 (mT/mGFP), 4 (IIA$^{fl/fl}$), and 5 (IIA/IIB$^{fl/fl}$ and IIB$^{fl/fl}$) animals.

few seconds with respect to LF (Fig. 3 and Video 4), marking the onset of the integration of the granules. As the motor domain of both NMII heavy chains contains a well-characterized actin-binding site (Furch et al., 1998; Murphy and Spudich, 1999), we reasoned that NMII could be recruited onto the fused granules by the newly assembled actin filaments. To test this hypothesis, we disrupted F-actin assembly by either cytochalasin D (CytoD; Fig. 4) or Latrunculin A (LatA; Fig. S4 A). As previously reported, these treatments do not affect the fusion of the granules with the APM but do induce a significant expansion of granules and block their integration (Masedunskas et al., 2011a). We confirmed that all the enlarged granules detected in the acinar cells indeed originated from the APM, as they were labeled with the apical marker aquaporin 5 (Gresz et al., 2004) but not with $Na^+/K^+/2Cl^-$ cotransporter (NKCC1), a well-established basolateral marker (Fig. 4 A; Evans et al., 2000). Surprisingly, neither CytoD nor LatA treatments affected the recruitment of either endogenous NMIIA and NMIIB (Fig. 4 B) or GFP-NMIIA (Fig. 4, C and D; and Fig. S4 A) onto the granules, although their distribution was no longer homogenous but rather patchy (Fig. 4 B, green arrowheads). Experiments using GFP-NMIIB were inconclusive. Similar observations were made imaging the exocytosis of mucin-containing granules in the SGs of fruit flies that express LF-Ruby and either Zip-GFP or Sqh-GFP (i.e., heavy and light chain of the *Drosophila* myosin II, respectively; Fig. S4 B), a secretory model system that uses a similar actomyosin complex to complete exocytosis (Tran et al., 2015). One pos-

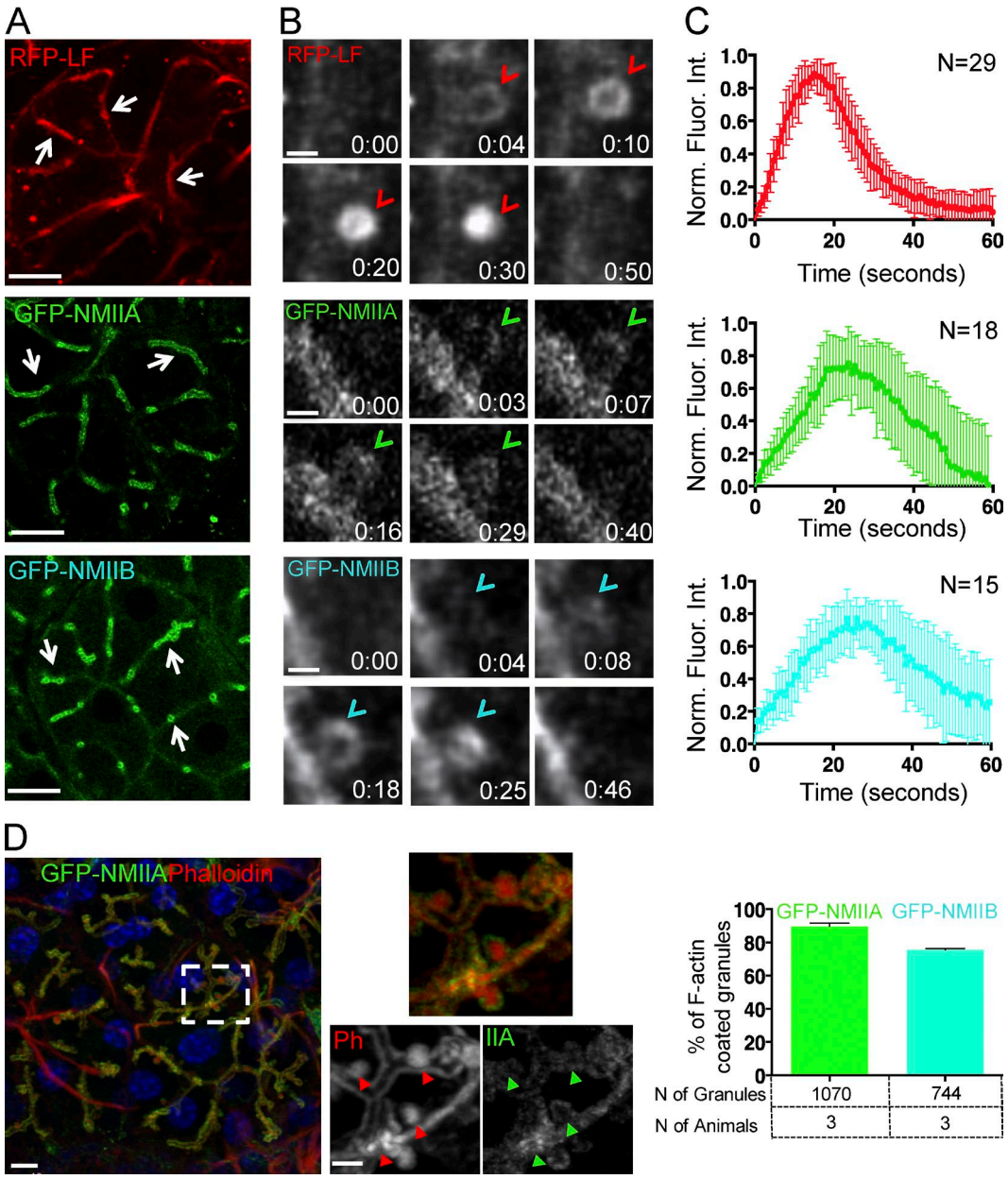

Figure 2. **Kinetics of recruitment of the actomyosin complex onto the secretory granules.** (A–C) ISMic of salivary acini in mice expressing RFP-LF (top), GFP-NMIIA (middle), and GFP-NMIIB (bottom). (A) Low magnification of individual acini shows the localization of LF, NMIIA, and NMIIB at the APM (arrows). Bars, 20 µm. (B) Time-lapse imaging of their recruitment onto the secretory granules (arrowheads). Bars, 1 µm. (C) Kinetics of RFP-LF, GFP-NMIIA, and GFP-NMIIB recruitment onto the secretory granules. The fluorescence intensity (Fluor. Int.) around the granules was measured during their integration, normalized (Norm.), and reported as a function of time, as described in Materials and methods. (Top and middle) Curves are means ± SD from one of three animals. N = number of granules. (D) Colocalization between NMII isoforms and F-actin. GFP-NMIIA (IIA) or GFP-NMIIB (not depicted) mice were injected with ISOP, and the SGs were excised after 10 min, fixed, and stained with Texas-Red Phalloidin (Ph; red). Bar, 6 µm. (Insets) A close up of the APM and the fused granules in the broken box. Arrowheads point to fused secretory granules. Bar, 2 µm. (Right) The percentage of phalloidin-labeled granules positive for either GFP-NMIIA or GFP-NMIIB (mean ± SD). *n* = 3 animals. NS by Student's *t* test.

sible explanation for these findings is that the effect of actin-disrupting agents is partial, allowing NMII isoforms to bind short residual actin filaments that still assemble on the granules. However, we are inclined to rule out this possibility based on the following evidence. First, in high-resolution z stacks of the enlarged CytoD-treated granules labeled with both GFP-NMIIA and phalloidin, we observed that patches of residual F-actin did not overlap with GFP-NMIIA (Fig. 4, D and E, bottom). Second, despite the expected significant decrease in the density of F-actin after CytoD treatment, we measured a two- to threefold increase in the levels of GFP-NMIIA on the enlarged granules with respect to control conditions (Fig. 4 E, top). Finally, using time-lapse imaging in GFP-NMIIA mice, we observed that the kinetics of the initial recruitment of GFP-NMIIA on the granules is not altered by the disruption of F-actin assembly (Fig. 4 F). Overall, our findings strongly suggest that F-actin does not play a key role in the recruitment of the NMII isoforms onto the secretory granules. This is con-

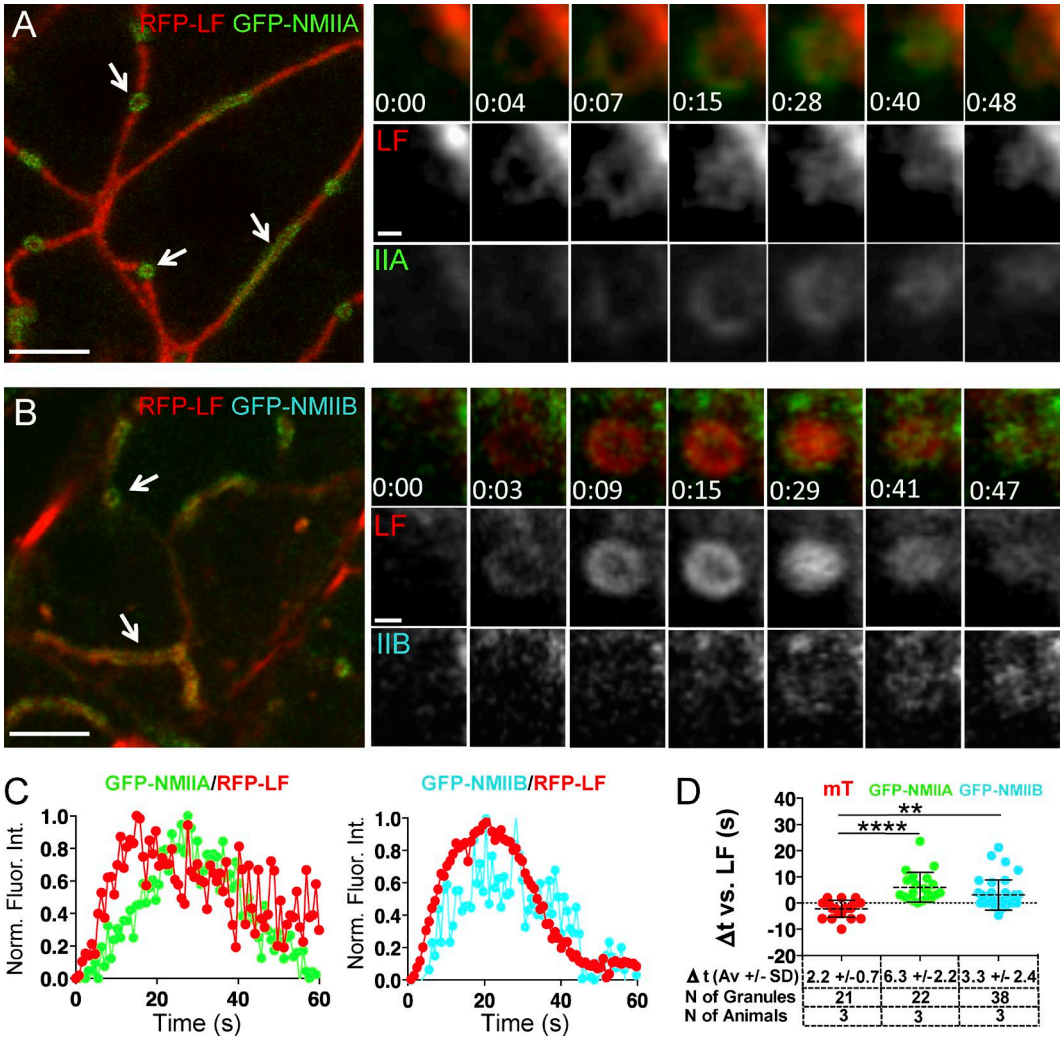

Figure 3. **F-actin assembly onto the secretory granules precedes the recruitment of NMIIA and NMIIB.** (A–D) ISMic of salivary acini in mice expressing RFP-LF and GFP-NMIIA (A, C, and D), GFP-NMIIB (B, C, and D), or mTomato (mT; D). (A and B, left) Low magnification of individual acini shows the localization of LF and the NMII isoforms at the APM (arrows). Bars, 10 µm. (Right) Time-lapse imaging of the recruitment of LF and the NMII isoforms onto the secretory granules after the injection of 0.03 mg/kg ISOP. Bars 1 µm. (C) Kinetics of the recruitment of RFP-LF and the NMII isoforms onto the secretory granules. Curves are from one representative granule (5–10 granules per animal, total of three animals). Norm. Fluor. Int., normalized fluorescence intensity. (D) The mean lag time ± SD between the appearance onto the fused secretory granules of LF and mT, GFP-NMIIA, or GFP-NMIIB was measured in mice expressing GFP-LF/mT (red dots), RFP-LF/GFP-NMIIA (green dots), and RFP-LF/GFP-NMIIB (cyan dots). **, $P < 0.01$; ****, $P < 0.0001$; ANOVA.

sistent with two recent studies: the first, in yeast, which shows that, during cytokinesis, NMII is recruited to the contractile ring by both IQGAP-Rng2 and anillin (Takaine et al., 2014), and the second, in *Drosophila*, which shows that, during morphogenesis, increased membrane tension is sufficient to promote the recruitment and activation of NMII at the cell cortex to regulate axis elongation (Fernandez-Gonzalez et al., 2009).

NMII bipolar filament assembly and activation is initiated by the phosphorylation of the NMII regulatory light chain (RLC) on S19 and T18, which induces a change in NMII conformation from a compact 10S assembly-incompetent to an extended 6S assembly-competent complex (Burgess et al., 2007; Jung et al., 2008). Intrigued by the observation that NMII appeared in discrete patches on the granule membrane upon disruption of F-actin assembly (Fig. 4, B and F; Fig. S4, arrows; and Video 5), we wanted to test whether these patches represented aggregates of folded/nonphosphorylated NMII molecules and whether F-actin is required to initiate the assembly and activation of bipolar NMII filaments.

To test this hypothesis, we first asked whether the RLC was phosphorylated during regulated exocytosis. Immunofluorescence showed that phosphorylated RLC was localized at the APM under resting conditions (Fig. S4) and on the fused F-actin–coated secretory granules upon ISOP stimulation (Fig. 5 A, left and middle, arrowheads and insets). Second, we investigated whether the RLCs of NMII on the fused granules were phosphorylated by myosin light chain kinase (MLCK; Hong et al., 2011). We found that, like phosphorylated RLC, MLCK localized in the cytoplasm under resting conditions (not depicted), whereas upon stimulation, it localized to 42 ± 2% of actin-coated secretory granules (mean ± SD, n = 600 granules scored in three animals; Fig. 5 A, right, arrowheads and inset). Next, we inhibited MLCK, via administration of ML-7 (Saitoh et al., 1987) through the salivary ducts, to determine the extent to which it regulates NMII during granule integration. We found that ML-7 treatment resulted in a significant delay in the integration of granule membranes into the APM and an initial expansion of

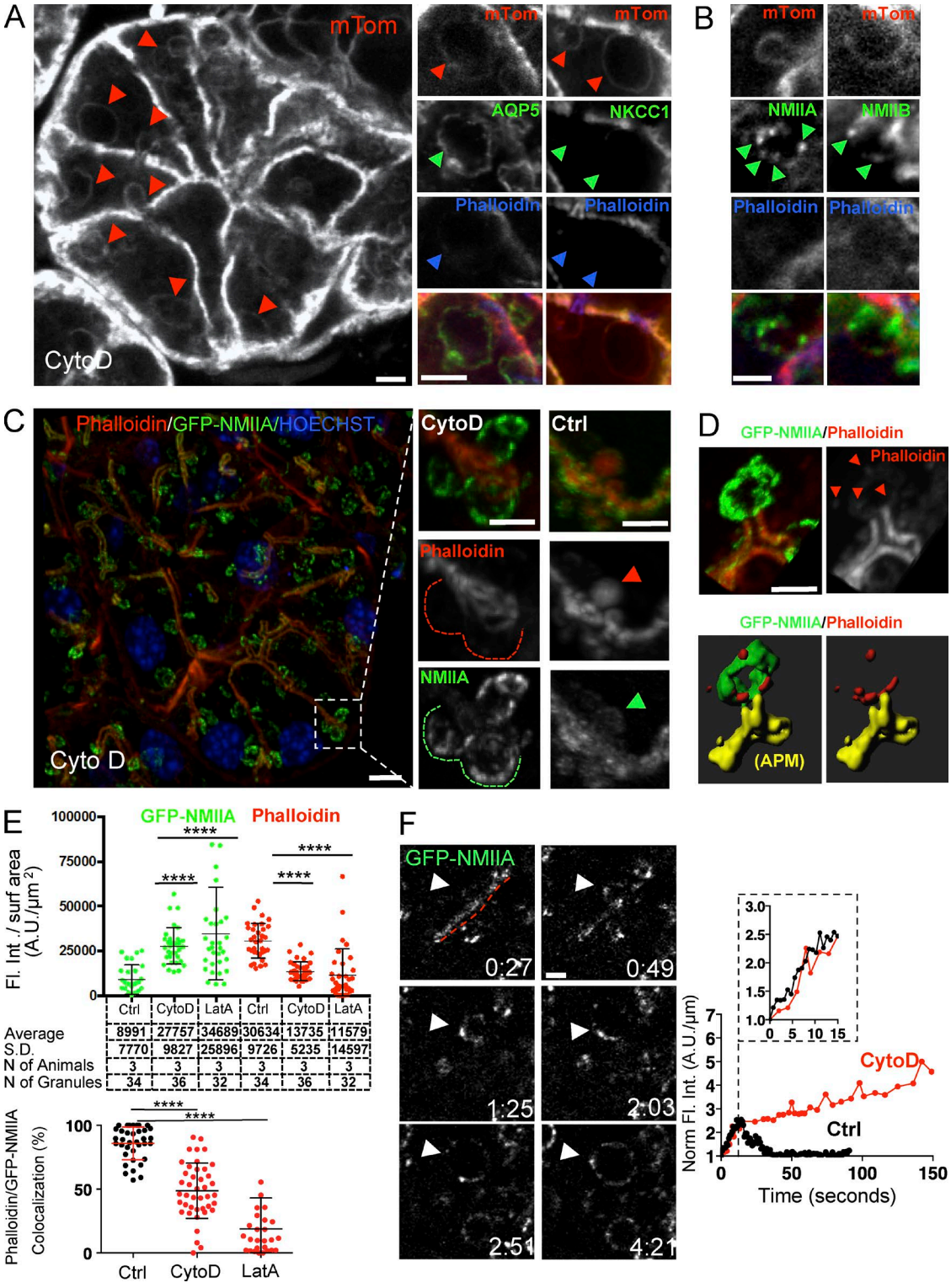

Figure 4. **NMIIA is recruited to the secretory granules independently of F-actin.** (A–F) Mice expressing either mTomato (mTom; A and B) or GFP-NMIIA (C–F) were exposed to 10 µM CytD for 10 min and injected SC with 0.03 mg/kg ISOP, as described in Materials and methods. (A and B) The SGs were explanted, processed for immunofluorescence, and labeled with Alexa Fluor 647 phalloidin and with antibodies directed against AQP5 (marker for the APM; A, middle), NKCC1 (marker for the basolateral plasma membrane; A, right), NMIIA (B, left), and NMIIB (B, right). (Left) Enlarged granules labeled with mTomato (red arrowheads). Bar, 3 µm. The series of small panels show high magnification of individual enlarged granules labeled for AQP5 but not NKCC1 (A, green arrowheads), phalloidin (A, blue arrowheads), and NMIIA and NMIIB (B, green arrowheads). Bars, 3 µm. (C–E) The SGs were explanted and labeled with Texas-Red phalloidin (red) and Hoechst (blue). (C, left) Maximal projection of a z stack. Bar, 5 µm. (Middle) The insets show a high magnification of the enlarged granules fused with the APM (dashed lines). Note that phalloidin staining is not detectable. (Right) The insets show fused granules under control conditions (arrowheads). Bars, 3 µm. (D) Maximal projection of a z stack in which phalloidin was detected (top, arrowheads). (Bottom) Isosurfaces generated as described in Materials and methods that show that GFP-NMIIA (green) does not overlap with the residual F-actin (red) on the enlarged granules. Bar, 3 µm. (E) Levels of GFP-NMIIA and phalloidin on the secretory granules after treatment with CytoD or LatA (top) and their

the granules (Fig. 5 C). These defects in granule integration were similar to those observed in the absence of NMIIA and/or NMIIB, most closely recapitulating the phenotype of the $IIB^{fl/fl}$ mice. This indicates that MLCK is required for activation of NMII on secretory granules.

Interestingly, whereas the level of the phosphorylated NMII on the granules was reduced after ML-7 treatment, as expected, the recruitment of NMIIA on the secretory granules was not affected (Fig. 5 B), indicating that NMII may indeed be targeted to fused granules in a 10S complex. Finally, we observed a reduction of both NMII RLC phosphorylation (Fig. 5 D, arrowheads) as well as MLCK (Fig. 5 E, arrowheads) after CytoD treatment. This is consistent with the fact that MLCK possesses a series of well-characterized F-actin binding sites (Hatch et al., 2001). Collectively, these data suggest that, during regulated exocytosis, NMII is recruited to fused secretory granules in an inactive state and that F-actin plays a key role in controlling the machinery regulating the assembly and activation of NMII filaments via the recruitment of MLCK. This is interesting as, in SGs, β-adrenergic stimulation activates primarily cAMP and PKA signaling pathways (Inagaki et al., 2010) rather than the canonical Ca^{2+}/calmodulin pathway, which controls the activation of MLCK in other systems (Kamm and Stull, 2011). The role of Ca^{2+}-independent regulation of nonmuscle NMII contractility has been poorly understood and primarily investigated in endothelial cells, where it was reported to play either an inhibitory (Goeckeler and Wysolmerski, 2005) or stimulatory role (Raina et al., 2009). Therefore, future investigations of the role of cAMP/PKA signaling in MLCK activation during regulated exocytosis will provide an improved understanding of this process.

In summary, here, we have begun to dissect the steps of the assembly of an actomyosin complex in live animals and to unravel the coordinated role of two NMII isoforms during membrane remodeling. We showed that F-actin is the first component assembled onto the membranes of the secretory granules, followed by the NMII isoforms, which are recruited independently of F-actin via a not yet identified mechanism. Notably, our study strongly suggests that F-actin provides a scaffold that can be used to transduce myosin-driven contractions and a signaling platform to recruit crucial components that initiate the assembly and activation of NMII filaments and possibly their disassembly. Because of the resolution limit of light microscopy, we could not determine whether NMIIA and NMIIB are assembled in hetero- or homofilaments or whether they show a distinct localization on the secretory granules. Nonetheless, our data support the notion that NMIIA and NMIIB play different roles during the integration process that likely require two distinct but coordinated steps, depicted in a model (Fig. 5 F) based on both data and speculation. The first is regulated by NMIIB, which stabilizes the membranes of the granules after fusion. We speculate that NMIIB may play an active role by driving the membranes toward the APM and/or facilitating F-actin depolymerization. The second is regulated by NMIIA, which is required to complete the integration process. One possibility is that it controls the progressive expansion of the fusion pore (Fig. 5 F). This model is consistent with the different enzymatic properties of these two NMII isoforms. Indeed, NMIIA has been shown to induce a higher contraction rate on actin filaments than NMIIB (Kovács et al., 2003; Heissler and Manstein, 2013), thus making it more suitable to regulate fast processes such as the opening and closing of the fusion pore, as suggested for neuroendocrine cells and the exocrine pancreas (Doreian et al., 2008; Neco et al., 2008; Bhat and Thorn, 2009). It is also possible that NMIIA controls plasma membrane tension, which, as shown in recent studies, regulates the integration of secretory vesicles (Bretou et al., 2014; Wen et al., 2016). However, NMIIB has a higher duty ratio than NMIIA and behaves as a cross-linker that generates prolonged tension on actin filaments (Wang et al., 2003; Heissler and Manstein, 2013), thus being more suitable for slower but more sustained contractions. However, we cannot completely rule out that NMIIB controls the dynamics of the fusion pore, as the expansion of the granules could be caused by swelling of the cargo upon closure of the fusion pore.

To distinguish between these models, it is essential in the future to develop approaches to measure the biophysical properties of the membranes in live mice. For example, the dynamics of the fusion pore could be investigated by measuring the kinetics of the ingress of fluorescent probes of different sizes into the fused granules, as shown in rats (Masedunskas et al., 2011a) and ex vivo model systems (Larina et al., 2007). Unfortunately, this approach does not work in mice because of the small size of the salivary ducts, which prevents the effective delivery of the probes into the acinar canaliculi. Alternatively, the dynamics of the pore could be assessed by measuring the release of cargo molecules into the canaliculi. This will require the generation of transgenic mice expressing a fluorescently labeled cargo protein sorted into the secretory granules, similarly to what has been shown in *Drosophila* (Tran et al., 2015; Rousso et al., 2016). Measures of membrane tension by classical approaches (e.g., optical tweezers or atomic force microscopy) are not feasible in live animals because of the lack of direct access to the tissue. However, we envision that other biophysical parameters correlated with membrane tension, such as membrane mobility, could be measured in vivo by light microscopy approaches, such as FRAP, which has been already applied in live mice (Erami et al., 2016). In addition, it will be important to define the ultrastructure of the secretory granules during different stages of the integration and under different experimental conditions to gain information such as the local changes in the curvature and the size of the pore, thus providing the basis to model the forces necessary to drive this process.

Materials and methods

Animals and procedures

All experiments were approved by the National Institute of Dental and Craniofacial Research Animal Care and Use Committee. Wild-type C57BL/6 and mT/mGFP mice were purchased from Jackson Laboratory. GFP-LF and RFP-LF mice were a gift from R.W. Soldner (University of Münster, Münster, Germany). GFP-NMIIA and GFP-NMIIB

colocalization (bottom). Error bars represent SD. ****, $P < 0.0001$; ANOVA. Ctrl, control; Fl. Int., fluorescence intensity. (F, left) ISMic of GFP-NMIIA recruitment onto the enlarged secretory granules (arrowheads) fused at the APM (red dashed line). Bar, 1 µm. (Right) Representative curves of the kinetics of recruitment of GFP-NMIIA in control (black curves) and CytoD-treated (red curves) mice. Curves are from one representative granule (5–10 granules per animal, total three animals). Norm., normalized.

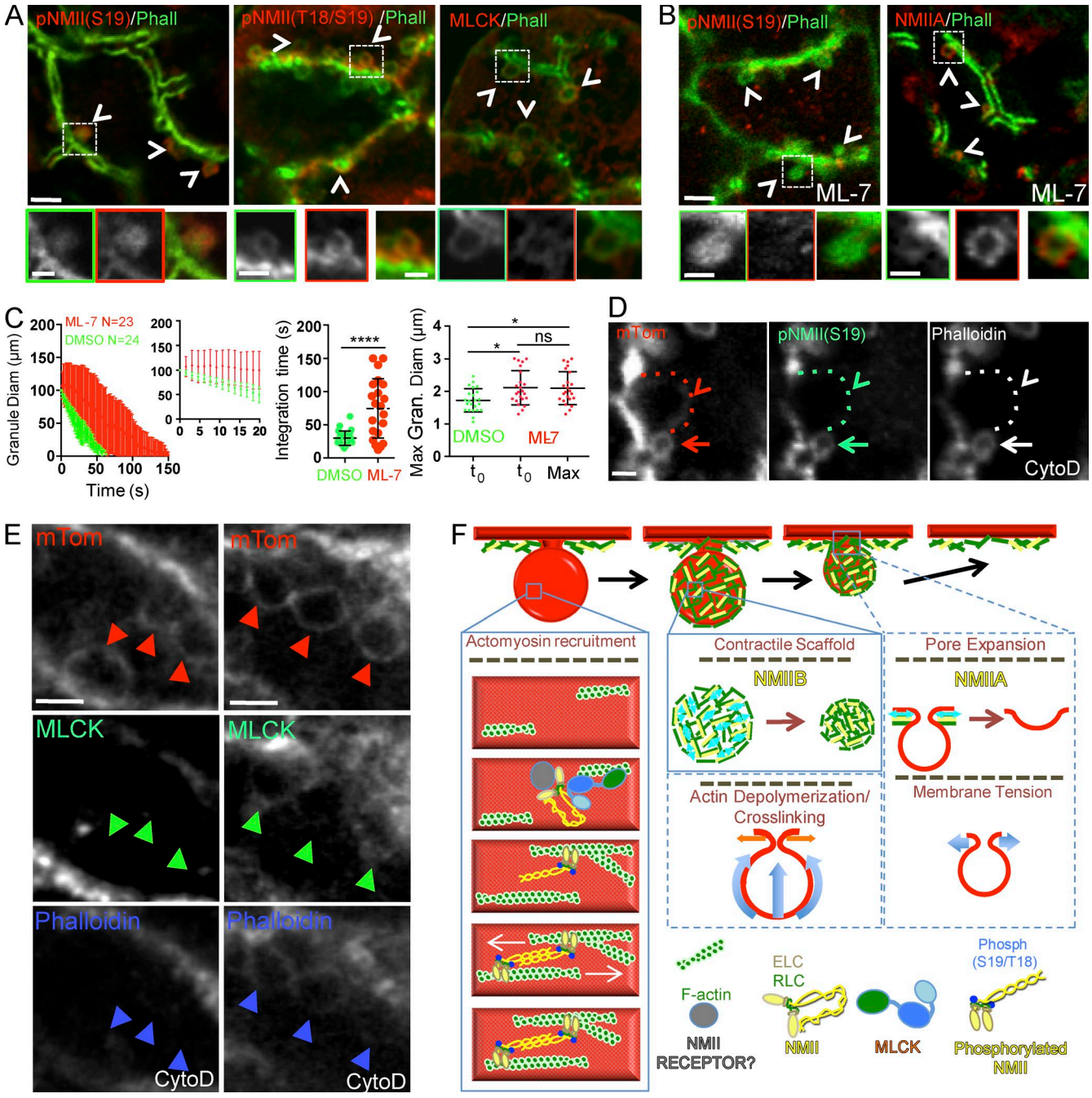

Figure 5. **F-actin recruits MLCK onto fused secretory granules to promote NMII RLC phosphorylation.** (A–E) Wild-type (A and B) or mTomato (mTom; C, D, and E) mice were left untreated (A) or treated with either 10 µM ML-7 (B and C) or 10 µM CytoD (D and E). Mice were injected with 0.03 mg/kg ISOP, and the SGs were either processed for indirect immunofluorescence (A, B, D, and E) or imaged in time-lapse modality (C). (A and B) Localization of the phosphorylated forms of NMII RLC, MLCK, and NMIIA (red; arrowheads and insets) onto the fused secretory granules revealed by Alexa Fluor 488–phalloidin (Phall) staining (green; arrowheads and insets). Bars: (top) 2 µm; (insets) 1 µm. (C) Quantitative analysis of the integration of the secretory granules in mice treated with ML-7 (red symbols) or DMSO (green symbols). (Left) The diameter (Diam) of the granules (Gran.) was measured during membrane integration and reported as a function of time. N = number of granules in three animals. (Middle left) Fitted curves were also generated. Maximum (Max) diameter (middle right) and the integration time (right) were estimated as described in the Materials and methods. Error bars represent SD. *, $P < 0.05$; ANOVA; ****, $P < 0.0001$; Student's *t* test. (D) Phosphorylated RLC is recruited on F-actin–coated secretory granules (arrows) but not on expanded secretory granules lacking F-actin (arrowheads and dotted lines). Bars, 2 µm. (E) MLCK recruitment on the expanded granules varies with the levels of F-actin. (Left) Expanded granules lacking both phalloidin and MLCK staining (arrowheads). (Right) Expanded granules with low levels of MLCK and phalloidin (arrowheads). Bars, 3 µm. (F) Proposed model of assembly of the actomyosin complex and role of the two NMII isoforms, based on data from this study (solid blue lines) and speculation (dashed blue lines). F-actin is assembled onto the membrane of the granules, and NMII isoforms are recruited via a not yet defined mechanism. F-actin recruits MLCK, which phosphorylates the RLC initiating the formation of NMII filaments, which in turn bind to F-actin. NMIIB generates sustained contraction on the F-actin scaffold (light blue double arrows), and the resulting forces drive the membranes of the granules into the APM (light blue arrows). This process may be also driven by F-actin cross-linking and depolymerization. NMIIA may generate contractions (light blue double arrows) that facilitate the expansion of the fusion pore (light blue arrows). Alternatively, NMIIA may directly or indirectly control plasma membrane tension and regulate the integration. ELC, essential light chain.

knock-in mice and homozygous floxed NMIIA ($IIA^{fl/fl}$), NMIIB ($IIB^{fl/fl}$), or NMIIA/NMIIB ($IIA/IIB^{fl/fl}$) mice were generated as described previously (Bao et al., 2007; Masedunskas et al., 2012a; Zhang et al., 2012). These mice were crossed according to Fig. S1 and Table 1, and PCR was used to confirm their genotypes.

All the mice (males and females) used in this study weighed 20–40 g. They were brought from the vivarium into the laboratory at least 2 d before the experiments and fed chow and water ad libitum. Mice were anesthetized by an i.p. injection of a mixture of 100 mg/kg ketamine and 20 mg/kg xylazine. The submandibular SGs were externalized, and the body temperature of the animals was controlled and maintained at 37–38°C, as previously described (Masedunskas et al., 2011a). We imaged a minimum of three animals per condition tested. This ensured us to score: (a) 5–10 exocytic events per animal in time-lapse imaging experiments, (b) 200–300 fused secretory granules per animal in immunofluorescence experiments, and (c) 15–30 fused granules per animals in Z scan. Randomization or blinding was not used in this study.

Adeno-Cre production

The adenovirus plasmid expressing Cre recombinase was developed using the ViraPower Adenoviral Expression System, which utilizes Gateway cloning technology (Life Technologies). Forward and reverse primers were synthesized to amplify just the CreGFP from the pCAG-Cre:GFP plasmid (plasmid 13776; Addgene) for the subsequent BP (PCR fragment + donor vector = entry clone) and LR (entry clone + destination vector = expression clone) reaction with the ViraPower plasmid. The plasmid was subsequently digested by a Pac1 endonuclease (New England Biolabs) and transfected into HEK-293a cells at 70–80% confluency in 15–25-cm Petri dishes using Turbofect transfection reagent (Life Technologies) for adenovirus production. 2–3 d later, the cells were lysed and added to the media, and the mixture was used to purify and concentrate the virus to ∼0.2–0.6 × 10^{13} viral particles/ml using a Vivapure AdenoPACK 500 kit (VS-AVPQ501; Sartorius Stedim). Viral particles were stored at −80°C in a buffer containing glycerol.

Adenovirus and drug delivery into the mouse submandibular SGs

Anesthetized mice were positioned in a previously described custom-made device (Masedunskas et al., 2011a) to hold the mouth open under a stereomicroscope. The submandibular salivary ducts (Wharton's ducts) located below the tongue were slightly enlarged by inserting flexible metallic cannulae, which were rapidly removed and replaced by tail vein catheters (BrainTree Scientific). The catheters were connected to a sterile syringe loaded with either the adenovirus (∼10^9–10^{10} particles/gland in sterile saline) or the drug diluted at the appropriate concentration. To prevent damaging the glands, the injections were performed using a PHD Ultra Nanomite syringe pump (Harvard Apparatus) with a flow rate of 2 µl/min and not exceeding a total volume of 45–50 µl per gland.

For the Ade-Cre delivery, the mice were placed back in their cages after the injections. Although Cre expression was detected after 2 d, substantial reductions in the levels of NMIIA and NMIIB were reached after 12–14 d (Fig. S2) after the injections. The efficiency of adenoviral-mediated expression in the acinar cells, although limited to one to three cells per field of view, was sufficient to perform time-lapse imaging and quantitative analysis. Drugs were all injected at the appropriate doses 20 min before the stimulation with ISOP, using DMSO as a control.

Indirect immunofluorescence

Fluorescent staining was performed by various protocols, depending on the antibody used, as described in Table 2.

Cardiac fixation. To preserve the subcellular architecture of the acinar cells, the SGs were fixed by cardiac perfusion using a solution consisting of 0.05% glutaraldehyde and 4% formaldehyde in 0.2 M Hepes buffered at a pH of 7.3. Cardiac perfusion was performed as follows: the left ventricle of the heart was punctured, and saline was injected to wash out the blood from the right atrium, followed by 30–35 ml of the fixative prewarmed to 37°C. Once the glands were fixed, they were excised, sliced into 150–200-µm sections in 1× PBS 7.4 using a vibratome (VT1000s; Leica), placed in fixative overnight at 4°C, washed in 1× PBS 7.4, and then stained. The immunostaining procedure after cardiac fixation involved the following steps: (a) blocking in 10% FBS and 0.02% saponin in PBS (blocking solution) for 30–45 min at RT, (b) incubation with primary antibodies in blocking solution for 2 d at 4°C, (c) staining with secondary antibodies in blocking solution overnight at 4°C, (d) if needed, staining with either phalloidin or HOESCHT for 30–60 min at RT, and (e) mounting each section on a glass slide with no. 1.5 coverslips for confocal imaging. In some cases, glutaraldehyde was omitted from the fixative to improve the antigenicity of the antibodies, provided that the structure of the acini was not significantly altered.

Snap freezing. Alternatively, SGs were excised, embedded in optimal cutting temperature compound (Tissue-Tek), and snap frozen in isopentane cooled in liquid nitrogen. Afterward, frozen tissue blocks were cut in 10–15-µm sections using a cryostat (CM3050S; Leica) at –20°C, adhered to silane-coated glass slides, and stained. The staining procedure involved first fixing each section by incubating it with the fixative solution for 15 min at RT. The staining involved the following steps: (a) incubation with blocking solution for 30–45 min at RT, (b) incubation with primary antibodies in blocking solution overnight 4°C, (c) staining with secondary antibodies in blocking solution for 1 h at room temperature, (d) if needed, staining with either phalloidin or HOESCHT for 30–60 min at RT, and (e) mounting each section on a glass slide and sealing each section with a no. 1.5 coverslip for confocal imaging.

Whole-mount staining in CytoD- and LatA-treated mice. The SGs of GFP-NMIIA mice were exposed and bathed for 20 min with 10 µM CytoD or LatA in saline maintained at 37°C and injected with 0.01 mg/kg ISOP SC. After 10 min for CytoD and 20 min for LatA, the glands were excised, fixed with 4% formaldehyde in 0.2 M Hepes buffered at a pH of 7.3 for 24 h at 4°C. The drugs penetrate into the tissue only for few hundreds of micrometers from the surface of the glands. Therefore, we sectioned them with the vibratome to generate: (a) slices with one side exposed to the drug (treatment) and (b) slices that were not exposed to the drug (control). All the slices were stained under the same conditions with phalloidin or HOESCHT for 30–60 min.

ISMic

In the anesthetized mice, the submandibular glands were exposed by a small longitudinal incision in the submandibular region. Using forceps, the connective tissue was separated from the glands without injuring the parenchyma. The exposed glands were gently pulled out without damaging them and without severing the blood vessels and the nerves. During the procedure, the glandular tissue was constantly moistened by applying saline. The anesthetized mice were placed on the preheated stage of a microscope and covered with a heated pad (37°C) to maintain body temperature. The externalized SGs were accommodated on a coverslip mounted on the stage above the objective. The glands and the body of the animal were immobilized using custom-made holders as previously shown (Masedunskas et al., 2011a). The blood flow was assessed visually by using the eyepiece. Animals with impaired blood flow were excluded from the analysis. Only acini-close blood vessels were imaged.

Table 1. **List of mice generated by crossing and used in this study**

Strain 1	Strain 2	Allele1/Allele2
GFP-LF	mT/mGFP	Het/Hom
GFP-NMIIA	RFP-LF	Hom/Het
GFP-NMIIB	RFP-LF	Hom/Het
$IIA^{fl/fl}$	mT/mGFP	Hom/Hom
$IIB^{fl/fl}$	mT/mGFP	Hom/Hom
$IIA/IIB^{fl/fl}$	mT/mGFP	Hom/Hom

Abbreviations used: Het, heterozygous; Hom, homozygous.

Microscope and imaging parameters

ISMic and indirect immunofluorescence were performed by a point-scanning IX81 inverted confocal microscope equipped with a scanning head (Fluoview 1000; Olympus America Inc.). All images were acquired using a Plan Apo 60× N.A. 1.42 oil immersion objective (Olympus America Inc.). Fluorophores were imaged using the appropriate lasers as required by their excitation spectra (excitation at 405, 488, 561, or 633 nm). Fluorophores with slightly overlapping emission ranges were imaged using the sequential scanning mode to avoid bleed through. The optimal focal plane for imaging the acinar cells was set at ∼15 µm below the surface of the gland, as determined by visualization of the collagen capsule that surrounded the acinar cells. For intravital microscopy specifically, the acquisition speed was ∼0.765 s/frame, and the pinhole was optimally set to 0.9 µm. z stacks were acquired at 0.25 or 0.50 µm apart going deeper into the section or tissue. During acquisition, any x-, y-, or z-axis drifts were manually corrected.

Image analysis and quantitation

Before quantification, all the time-lapse videos were processed by digital image stabilization, which was performed using linear alignment using the Stackreg plugin in ImageJ (National Institutes of Health). Stabilization significantly minimized any distortions from motion artifacts created during ISMic. Data analysis and graphics were done in Prism (GraphPad) and Excel (Microsoft), and the images were assembled in Photoshop (Adobe).

Diameter of the secretory granules. The diameters of the secretory granules were estimated in mice expressing the mT/mGFP reporter. They were identified as circular profiles at the APM labeled by either mT or mGFP. Diameters were measured in time series from the frame the profiles of the granules were clearly visible, which typically occurs 5–10 s after the opening of the fusion pore. The diameters were reported as a function of time, and in Figs. 1 and 4, time 0 corresponds to three frames before the beginning of the integration into the APM. Finally, the maximal diameters during the integration were calculated for each condition. Results are reported as mean ± SD. Statistical significance among different conditions was calculated using ANOVA.

Fluorescence intensity in time-lapse experiments. The secretory granules fused at the APM were identified by the specific fluorescent marker analyzed, and a circular region of interest was drawn around them using ImageJ. The normalized fluorescent intensity was measured and plotted as a function of time. Time 0 was assigned to the frame before the one in which the intensity of the first fluorescent marker analyzed rose above background levels. As mice and granules exhibited different levels of fluorescence, the measured intensities were normalized in a way that 1 was assigned to the maximum value and 0 to the background. For each mouse expressing a single fluorescent maker, the values of the fluorescent intensity for a given time point were averaged and reported as mean ± SD. For mice expressing two fluorescent markers, we reported the curves for one representative granule. For all the experiments, 5–10 granules per animal were analyzed for a total of three to five animals. The $t_{1/2}$ of the recruitment of GFP-LF, RFP-LF, GFP-NMIIA, and GFP-NMIIB onto the secretory granules was calculated.

Fluorescence intensity in z stacks. Z stacks were acquired by confocal microscopy using the same laser power and detector settings for controls and treatments. Volume rendering and surface area were generated with Imaris software (Bitplane) using the isosurface tool. The integrated density of the fluorescent levels per granule was estimated using Imaris or FIJI software.

Fluorescence colocalization analysis. Fiji software was used for colocalization analysis. Images were manually thresholded, and an image containing the overlapping pixels (GFP-NMIlA and phalloidin) was generated using the multiply feature in the image calculator function. Finally, individual fused SGs were outlined, and the overlapping integrated fluorescence intensity was divided by the integrated fluorescence intensity of GFP-NMIlA to calculate percent colocalization.

Drosophila experiments

Fly strains and genetics. The following *Drosophila* lines were used: Bloomington no. 35545 (*y^1 w**; *P{UAS-Lifeact-Ruby}VIE-19A*), no. 58362 (*w**; *P{UASt-Lifeact-RFP}3*), and no. *57144* (*y^1 w**; *sqh-GFP.RLC}2*). Bloomington no. 35545 was recombined with Flytrap line no. CC01626 to generate *Zip-GFP* and *UAS-Lifeact-Ruby*. The Gal4 driver line used in these studies was Bloomington stock no. 6978 (*w^{1118}*; *P{GawB}c135)*, which drives expression in the *Drosophila* SG beginning during embryonic stage 15 and continuing through the third instar larval stage. The *c135-Gal4* driver was recombined with Bloomington no. 58362 to generate *c135-Gal4> UAS-Lifeact-RFP*. All *Drosophila* crosses were kept on MM media (KD Medical, Inc.) at 25°C unless specified otherwise.

Ex vivo *Drosophila* SG culture and real-time imaging. Secreting SGs from third instar larvae were dissected in Schneider's *Drosophila* medium (Gibco) and transferred to glass-bottom culture dishes (MatTek) containing 50 µl of media. Then, the majority of the media was removed from the dish and a 13-mm, 0.05-µm, polycarbonate membrane filter (Sterlitech) was gently placed on top of the gland. The media that was removed from the dish was then placed on top of the

Table 2. **List of antibodies used in this study**

Antibody/Probe	Species	Source	Protocol	Dilution	Figure
Phospho-NMII (S19)	Rabbit	Cell Signaling no. 3671	Snap freezing, cardiac fixation	1:50	4A, S4
Phospho-NMII (S19T18)	Rabbit	Cell Signaling no. 3674	Snap freezing, cardiac fixation	1:50	4A, S4
NMIIA–heavy chain	Rabbit	BioLegend no. 909801	Snap freezing, cardiac fixation	1:50	4A, S2
NMIIB–heavy chain	Rabbit	BioLegend no. 909901	Snap freezing, cardiac fixation	1:50	S2
NMIIC–heavy chain	Rabbit	BioLegend 19192	Snap freezing, cardiac fixation	1:50	S3
MLCK (Clone K36)	Mouse	Sigma-Aldrich	Snap freezing, cardiac fixation	1:50	4A, S3
Alexa 488–phalloidin, Alexa 594–phalloidin, Alexa 647–phalloidin		Molecular Probes	Snap freezing, cardiac fixation, whole mount	1:200	2D, 3B, 4A, 4B, 4D

membrane filter, and LatA (final concentration 3 µM) or CytoD (final concentration 10 µM) was added to the media resting on top of the polycarbonate membrane immediately before imaging. All glands were imaged on a confocal microscope (A1R+; Nikon) with a CFI Lambda S Apo LWD 40×/1.15 NA WI objective.

Online supplemental material

Fig. S1 describes the membrane/Cre reporter mice and the generation of floxed NMII mice expressing the Cre reporter. Fig. S2 describes the quantification of the NMIIA and NMIIB levels in mt/mGFP, $IIA^{fl/fl}$, $IIB^{fl/f}$, and $IIA\text{-}IIB^{fl/f}$ mice. In addition, it shows some representative curves of the kinetics of integration of the secretory granules reported in Fig. 1. Fig. S3 describes the kinetics of recruitment of the actomyosin cytoskeleton onto the secretory granules. Fig. S4 describes the recruitment of NMII onto secretory granules despite inhibition of F-actin in mice and *Drosophila* and the phosphorylation of NMII light-chain kinase under resting conditions. Video 1 shows the integration of secretory granules into the APM in mice lacking NMIIA, NMIIB, or both. Video 2 shows the kinetics of recruitment of GFP-LF and RFP-LF onto the secretory granules fused with the APM. Video 3 shows the recruitment of GFP-NMIIA and GFP-NMIIB onto the secretory granules fused with the APM. Video 4 shows the delay of recruitment of GFP-NMIIA and GFP-NMIIB onto the secretory granules fused with the APM with respect to F-actin. Video 5 shows the recruitment of GFP-NMIIA onto the secretory granules fused with the plasma membrane when F-actin assembly is prevented by CytoD.

Acknowledgments

We would like to thank Drs. Julie Donaldson, John Hammer, Bechara Kachar, Paul Randazzo, and Jim Sellers for critical reading of the manuscript.

This research was supported by the Intramural Research Program of the National Institutes of Health, National Cancer Institute (grant ZIA BC 011682), Center for Cancer Research and the National Institute of Dental and Craniofacial Research.

The authors declare no competing financial interests.

Author contributions: R. Weigert designed the experiments. O. Milberg, A. Shitara, A. Masedunskas, M. Tora, and S. Ebrahim performed the experiments. Y. Chen and R. Weigert analyzed the experiments. D.T. Tran and K.G. Ten Hagen designed and performed the experiments in *Drosophila*. M.A. Conti and R.S. Adelstein generated floxed and GFP-NMII mice. R. Weigert and S. Ebrahim wrote the manuscript. All authors read and approved the final manuscript.

Submitted: 21 December 2016
Revised: 2 April 2017
Accepted: 2 May 2017

References

Bao, J., X. Ma, C. Liu, and R.S. Adelstein. 2007. Replacement of nonmuscle myosin II-B with II-A rescues brain but not cardiac defects in mice. *J. Biol. Chem.* 282:22102–22111. http://dx.doi.org/10.1074/jbc.M702731200

Bhat, P., and P. Thorn. 2009. Myosin 2 maintains an open exocytic fusion pore in secretory epithelial cells. *Mol. Biol. Cell.* 20:1795–1803. http://dx.doi.org/10.1091/mbc.E08-10-1048

Bretou, M., O. Jouannot, I. Fanget, P. Pierobon, N. Larochette, P. Gestraud, M. Guillon, V. Emiliani, S. Gasman, C. Desnos, et al. 2014. Cdc42 controls the dilation of the exocytotic fusion pore by regulating membrane tension. *Mol. Biol. Cell.* 25:3195–3209. http://dx.doi.org/10.1091/mbc.E14-07-1229

Burgess, S.A., S. Yu, M.L. Walker, R.J. Hawkins, J.M. Chalovich, and P.J. Knight. 2007. Structures of smooth muscle myosin and heavy meromyosin in the folded, shutdown state. *J. Mol. Biol.* 372:1165–1178. http://dx.doi.org/10.1016/j.jmb.2007.07.014

Burgoyne, R.D., and A. Morgan. 2003. Secretory granule exocytosis. *Physiol. Rev.* 83:581–632. http://dx.doi.org/10.1152/physrev.00031.2002

Chiaruttini, N., L. Redondo-Morata, A. Colom, F. Humbert, M. Lenz, S. Scheuring, and A. Roux. 2015. Relaxation of loaded ESCRT-III spiral springs drives membrane deformation. *Cell.* 163:866–879. http://dx.doi.org/10.1016/j.cell.2015.10.017

Crish, J., M.A. Conti, T. Sakai, R.S. Adelstein, and T.T. Egelhoff. 2013. Keratin 5-Cre-driven excision of nonmuscle myosin IIA in early embryo trophectoderm leads to placenta defects and embryonic lethality. *Dev. Biol.* 382:136–148. http://dx.doi.org/10.1016/j.ydbio.2013.07.017

Daley, W.P., and K.M. Yamada. 2013. ECM-modulated cellular dynamics as a driving force for tissue morphogenesis. *Curr. Opin. Genet. Dev.* 23:408–414. http://dx.doi.org/10.1016/j.gde.2013.05.005

Doreian, B.W., T.G. Fulop, and C.B. Smith. 2008. Myosin II activation and actin reorganization regulate the mode of quantal exocytosis in mouse adrenal chromaffin cells. *J. Neurosci.* 28:4470–4478. http://dx.doi.org/10.1523/JNEUROSCI.0008-08.2008

Erami, Z., D. Herrmann, S.C. Warren, M. Nobis, E.J. McGhee, M.C. Lucas, W. Leung, N. Reischmann, A. Mrowinska, J.P. Schwarz, et al. 2016. Intravital FRAP imaging using an E-cadherin-GFP mouse reveals disease- and drug-dependent dynamic regulation of cell-cell junctions in live tissue. *Cell Reports.* 14:152–167. http://dx.doi.org/10.1016/j.celrep.2015.12.020

Evans, R.L., K. Park, R.J. Turner, G.E. Watson, H.V. Nguyen, M.R. Dennett, A.R. Hand, M. Flagella, G.E. Shull, and J.E. Melvin. 2000. Severe impairment of salivation in $Na^+/K^+/2Cl^-$ cotransporter (NKCC1)-deficient mice. *J. Biol. Chem.* 275:26720–26726.

Ferguson, S.M., and P. De Camilli. 2012. Dynamin, a membrane-remodelling GTPase. *Nat. Rev. Mol. Cell Biol.* 13:75–88.

Fernandez-Gonzalez, R., S.M. Simoes, J.C. Röper, S. Eaton, and J.A. Zallen. 2009. Myosin II dynamics are regulated by tension in intercalating cells. *Dev. Cell.* 17:736–743. http://dx.doi.org/10.1016/j.devcel.2009.09.003

Furch, M., M.A. Geeves, and D.J. Manstein. 1998. Modulation of actin affinity and actomyosin adenosine triphosphatase by charge changes in the myosin motor domain. *Biochemistry.* 37:6317–6326. http://dx.doi.org/10.1021/bi972851y

Goeckeler, Z.M., and R.B. Wysolmerski. 2005. Myosin phosphatase and cofilin mediate cAMP/cAMP-dependent protein kinase-induced decline in endothelial cell isometric tension and myosin II regulatory light chain phosphorylation. *J. Biol. Chem.* 280:33083–33095. http://dx.doi.org/10.1074/jbc.M503173200

Gresz, V., T.H. Kwon, H. Gong, P. Agre, M.C. Steward, L.S. King, and S. Nielsen. 2004. Immunolocalization of AQP-5 in rat parotid and submandibular salivary glands after stimulation or inhibition of secretion in vivo. *Am. J. Physiol. Gastrointest. Liver Physiol.* 287:G151–G161. http://dx.doi.org/10.1152/ajpgi.00480.2003

Hatch, A.L., P.S. Gurel, and H.N. Higgs. 2014. Novel roles for actin in mitochondrial fission. *J. Cell Sci.* 127:4549–4560. http://dx.doi.org/10.1242/jcs.153791

Hatch, V., G. Zhi, L. Smith, J.T. Stull, R. Craig, and W. Lehman. 2001. Myosin light chain kinase binding to a unique site on F-actin revealed by three-dimensional image reconstruction. *J. Cell Biol.* 154:611–618. http://dx.doi.org/10.1083/jcb.200105079

Heissler, S.M., and D.J. Manstein. 2013. Nonmuscle myosin-2: mix and match. *Cell. Mol. Life Sci.* 70:1–21. http://dx.doi.org/10.1007/s00018-012-1002-9

Henne, W.M., H. Stenmark, and S.D. Emr. 2013. Molecular mechanisms of the membrane sculpting ESCRT pathway. *Cold Spring Harb. Perspect. Biol.* 5:a016766. http://dx.doi.org/10.1101/cshperspect.a016766

Hong, F., B.D. Haldeman, D. Jackson, M. Carter, J.E. Baker, and C.R. Cremo. 2011. Biochemistry of smooth muscle myosin light chain kinase. *Arch. Biochem. Biophys.* 510:135–146. http://dx.doi.org/10.1016/j.abb.2011.04.018

Inagaki, T., K. Ono, W. Masuda, T. Iida, R. Hosokawa, and K. Inenaga. 2010. Differences in the Ca^{2+} response resulting from neurotransmitter stimulations of rat parotid acini and ducts. *Auton. Neurosci.* 154:102–107. http://dx.doi.org/10.1016/j.autneu.2009.12.005

Jerdeva, G.V., K. Wu, F.A. Yarber, C.J. Rhodes, D. Kalman, J.E. Schechter, and S.F. Hamm-Alvarez. 2005. Actin and non-muscle myosin II facilitate apical exocytosis of tear proteins in rabbit lacrimal acinar epithelial cells. *J. Cell Sci.* 118:4797–4812. http://dx.doi.org/10.1242/jcs.02573

Jung, H.S., S. Komatsu, M. Ikebe, and R. Craig. 2008. Head–head and head–tail interaction: a general mechanism for switching off myosin II activity in cells. *Mol. Biol. Cell.* 19:3234–3242. http://dx.doi.org/10.1091/mbc.E08-02-0206

Kamm, K.E., and J.T. Stull. 2011. Signaling to myosin regulatory light chain in sarcomeres. *J. Biol. Chem.* 286:9941–9947. http://dx.doi.org/10.1074/jbc.R110.198697

Korobova, F., T.J. Gauvin, and H.N. Higgs. 2014. A role for myosin II in mammalian mitochondrial fission. *Curr. Biol.* 24:409–414. http://dx.doi.org/10.1016/j.cub.2013.12.032

Kovács, M., F. Wang, A. Hu, Y. Zhang, and J.R. Sellers. 2003. Functional divergence of human cytoplasmic myosin II: kinetic characterization of the non-muscle IIA isoform. *J. Biol. Chem.* 278:38132–38140. http://dx.doi.org/10.1074/jbc.M305453200

Kozlov, M.M., F. Campelo, N. Liska, L.V. Chernomordik, S.J. Marrink, and H.T. McMahon. 2014. Mechanisms shaping cell membranes. *Curr. Opin. Cell Biol.* 29:53–60. http://dx.doi.org/10.1016/j.ceb.2014.03.006

Larina, O., P. Bhat, J.A. Pickett, B.S. Launikonis, A. Shah, W.A. Kruger, J.M. Edwardson, and P. Thorn. 2007. Dynamic regulation of the large exocytotic fusion pore in pancreatic acinar cells. *Mol. Biol. Cell.* 18:3502–3511. http://dx.doi.org/10.1091/mbc.E07-01-0024

Masedunskas, A., M. Sramkova, L. Parente, K.U. Sales, P. Amornphimoltham, T.H. Bugge, and R. Weigert. 2011a. Role for the actomyosin complex in regulated exocytosis revealed by intravital microscopy. *Proc. Natl. Acad. Sci. USA.* 108:13552–13557. http://dx.doi.org/10.1073/pnas.1016778108

Masedunskas, A., M. Sramkova, and R. Weigert. 2011b. Homeostasis of the apical plasma membrane during regulated exocytosis in the salivary glands of live rodents. *Bioarchitecture.* 1:225–229. http://dx.doi.org/10.4161/bioa.18405

Masedunskas, A., N. Porat-Shliom, and R. Weigert. 2012a. Linking differences in membrane tension with the requirement for a contractile actomyosin scaffold during exocytosis in salivary glands. *Commun. Integr. Biol.* 5:84–87. http://dx.doi.org/10.4161/cib.18258

Masedunskas, A., N. Porat-Shliom, and R. Weigert. 2012b. Regulated exocytosis: novel insights from intravital microscopy. *Traffic.* 13:627–634. http://dx.doi.org/10.1111/j.1600-0854.2012.01328.x

Miklavc, P., E. Hecht, N. Hobi, O.H. Wittekindt, P. Dietl, C. Kranz, and M. Frick. 2012. Actin coating and compression of fused secretory vesicles are essential for surfactant secretion—a role for Rho, formins and myosin II. *J. Cell Sci.* 125:2765–2774. http://dx.doi.org/10.1242/jcs.105262

Miklavc, P., K. Ehinger, A. Sultan, T. Felder, P. Paul, K.E. Gottschalk, and M. Frick. 2015. Actin depolymerisation and crosslinking join forces with myosin II to contract actin coats on fused secretory vesicles. *J. Cell Sci.* 128:1193–1203. http://dx.doi.org/10.1242/jcs.165571

Milberg, O., M. Tora, A. Shitara, T. Takuma, A. Masedunskas, and R. Weigert. 2014. Probing the role of the actin cytoskeleton during regulated exocytosis by intravital microscopy. *Methods Mol. Biol.* 1174:407–421. http://dx.doi.org/10.1007/978-1-4939-0944-5_28

Murphy, C.T., and J.A. Spudich. 1999. The sequence of the myosin 50-20K loop affects Myosin's affinity for actin throughout the actin-myosin ATPase cycle and its maximum ATPase activity. *Biochemistry.* 38:3785–3792. http://dx.doi.org/10.1021/bi9826815

Muzumdar, M.D., B. Tasic, K. Miyamichi, L. Li, and L. Luo. 2007. A global double-fluorescent Cre reporter mouse. *Genesis.* 45:593–605. http://dx.doi.org/10.1002/dvg.20335

Neco, P., C. Fernández-Peruchena, S. Navas, L.M. Gutiérrez, G.A. de Toledo, and E. Alés. 2008. Myosin II contributes to fusion pore expansion during exocytosis. *J. Biol. Chem.* 283:10949–10957. http://dx.doi.org/10.1074/jbc.M709058200

Nightingale, T.D., I.J. White, E.L. Doyle, M. Turmaine, K.J. Harrison-Lavoie, K.F. Webb, L.P. Cramer, and D.F. Cutler. 2011. Actomyosin II contractility expels von Willebrand factor from Weibel-Palade bodies during exocytosis. *J. Cell Biol.* 194:613–629. http://dx.doi.org/10.1083/jcb.201011119

Pittet, M.J., and R. Weissleder. 2011. Intravital imaging. *Cell.* 147:983–991. http://dx.doi.org/10.1016/j.cell.2011.11.004

Porat-Shliom, N., O. Milberg, A. Masedunskas, and R. Weigert. 2013. Multiple roles for the actin cytoskeleton during regulated exocytosis. *Cell. Mol. Life Sci.* 70:2099–2121. http://dx.doi.org/10.1007/s00018-012-1156-5

Raina, H., J. Zacharia, M. Li, and W.G. Wier. 2009. Activation by Ca^{2+}/calmodulin of an exogenous myosin light chain kinase in mouse arteries. *J. Physiol.* 587:2599–2612. http://dx.doi.org/10.1113/jphysiol.2008.165258

Riedl, J., A.H. Crevenna, K. Kessenbrock, J.H. Yu, D. Neukirchen, M. Bista, F. Bradke, D. Jenne, T.A. Holak, Z. Werb, et al. 2008. Lifeact: a versatile marker to visualize F-actin. *Nat. Methods.* 5:605–607. http://dx.doi.org/10.1038/nmeth.1220

Riedl, J., K.C. Flynn, A. Raducanu, F. Gärtner, G. Beck, M. Bösl, F. Bradke, S. Massberg, A. Aszodi, M. Sixt, and R. Wedlich-Söldner. 2010. Lifeact mice for studying F-actin dynamics. *Nat. Methods.* 7:168–169. http://dx.doi.org/10.1038/nmeth0310-168

Rousso, T., E.D. Schejter, and B.Z. Shilo. 2016. Orchestrated content release from *Drosophila* glue-protein vesicles by a contractile actomyosin network. *Nat. Cell Biol.* 18:181–190. http://dx.doi.org/10.1038/ncb3288

Saitoh, M., T. Ishikawa, S. Matsushima, M. Naka, and H. Hidaka. 1987. Selective inhibition of catalytic activity of smooth muscle myosin light chain kinase. *J. Biol. Chem.* 262:7796–7801.

Shitara, A., and R. Weigert. 2015. Imaging membrane remodeling during regulated exocytosis in live mice. *Exp. Cell Res.* 337:219–225. http://dx.doi.org/10.1016/j.yexcr.2015.06.018

Shnyrova, A.V., V.A. Frolov, and J. Zimmerberg. 2009. Domain-driven morphogenesis of cellular membranes. *Curr. Biol.* 19:R772–R780. http://dx.doi.org/10.1016/j.cub.2009.07.063

Simunovic, M., and P. Bassereau. 2014. Reshaping biological membranes in endocytosis: crossing the configurational space of membrane-protein interactions. *Biol. Chem.* 395:275–283. http://dx.doi.org/10.1515/hsz-2013-0242

Sokac, A.M., C. Co, J. Taunton, and W. Bement. 2003. Cdc42-dependent actin polymerization during compensatory endocytosis in *Xenopus* eggs. *Nat. Cell Biol.* 5:727–732. http://dx.doi.org/10.1038/ncb1025

Sokac, A.M., C. Schietroma, C.B. Gundersen, and W.M. Bement. 2006. Myosin-1c couples assembling actin to membranes to drive compensatory endocytosis. *Dev. Cell.* 11:629–640. http://dx.doi.org/10.1016/j.devcel.2006.09.002

Sramkova, M., A. Masedunskas, L. Parente, A. Molinolo, and R. Weigert. 2009. Expression of plasmid DNA in the salivary gland epithelium: novel approaches to study dynamic cellular processes in live animals. *Am. J. Physiol. Cell Physiol.* 297:C1347–C1357. http://dx.doi.org/10.1152/ajpcell.00262.2009

Suetsugu, S., S. Kurisu, and T. Takenawa. 2014. Dynamic shaping of cellular membranes by phospholipids and membrane-deforming proteins. *Physiol. Rev.* 94:1219–1248. http://dx.doi.org/10.1152/physrev.00040.2013

Takaine, M., O. Numata, and K. Nakano. 2014. Fission yeast IQGAP maintains F-actin-independent localization of myosin-II in the contractile ring. *Genes Cells.* 19:161–176. http://dx.doi.org/10.1111/gtc.12120

Tran, D.T., A. Masedunskas, R. Weigert, and K.G. Ten Hagen. 2015. Arp2/3-mediated F-actin formation controls regulated exocytosis in vivo. *Nat. Commun.* 6:10098. http://dx.doi.org/10.1038/ncomms10098

Wang, F., M. Kovacs, A. Hu, J. Limouze, E.V. Harvey, and J.R. Sellers. 2003. Kinetic mechanism of non-muscle myosin IIB: functional adaptations for tension generation and maintenance. *J. Biol. Chem.* 278:27439–27448. http://dx.doi.org/10.1074/jbc.M302510200

Weigert, R., N. Porat-Shliom, and P. Amornphimoltham. 2013. Imaging cell biology in live animals: ready for prime time. *J. Cell Biol.* 201:969–979. http://dx.doi.org/10.1083/jcb.201212130

Wen, P.J., S. Grenklo, G. Arpino, X. Tan, H.S. Liao, J. Heureaux, S.Y. Peng, H.C. Chiang, E. Hamid, W.D. Zhao, et al. 2016. Actin dynamics provides membrane tension to merge fusing vesicles into the plasma membrane. *Nat. Commun.* 7:12604. http://dx.doi.org/10.1038/ncomms12604

Zhang, Y., M.A. Conti, D. Malide, F. Dong, A. Wang, Y.A. Shmist, C. Liu, P. Zerfas, M.P. Daniels, C.C. Chan, et al. 2012. Mouse models of MYH9-related disease: mutations in nonmuscle myosin II-A. *Blood.* 119:238–250. http://dx.doi.org/10.1182/blood-2011-06-358853